


Fusion-fission events in the $^{11}\text{B} + ^{181}\text{Ta}$ reaction up to 5.7 MeV/nucleon energy

Rinku Prajapat[ⓧ], Moumita Maiti^{ⓧ,*} and Deepak Kumar^{ⓧ†}

Department of Physics, Indian Institute of Technology Roorkee, Roorkee-247667, Uttarakhand, India

 (Received 19 October 2020; revised 8 December 2020; accepted 16 December 2020; published 11 January 2021)

Background: In heavy-ion fusion reactions, the compound nucleus' de-excitation process is observed via two competitive modes, evaporation of particles and fission, at relatively higher excitation energies. Although fusion-fission dynamics have been extensively studied in actinide nuclei, exploration of the same is yet to come for preactinide nuclei.

Purpose: The objective is to understand the fusion-fission dynamics involved in the $^{11}\text{B} + ^{181}\text{Ta}$ reaction within 4.8–5.7 MeV/nucleon energy by measuring absolute cross sections of the residues, which are mainly populating through complete and incomplete fusion-evaporation (FE), pre-equilibrium (PEQ), and fusion-fission (FF) mechanisms, as well as to infer on the mass and charge distributions of fission fragments.

Method: The stacked-foil activation technique was employed, followed by off-line γ -ray spectroscopy, to measure the activity and production cross sections of radionuclides populated through FE and FF. Charge and mass distributions were studied to obtain dispersion parameters of fission fragments.

Results: The equilibrium and pre-equilibrium reaction models have been used to analyze residual cross-section data resulting from FE and PEQ processes in the framework of EMPIRE3.2.2 and PACE4 codes. PEQ reaction's strengths in $3n$ -channel have been extracted and compared with other systems. The relative distribution of spins between the ground and isomeric state of ^{186}Ir has been discussed in view of the measured isomeric cross-section ratios. Further, 22 fission-fragments have been identified within the mass range $24 \leq A \leq 160$. The variance extracted from the measured isotopic yield distributions of Nd isotopes is in good agreement with the literature values. A well-consistent approach has been employed to determine the isobaric yield distribution of Nd and In isotopes.

Conclusion: The combination of Hauser-Feshbach formalism for compound evaporation and the Exciton model for PEQ reaction agrees with the measured data of xn -channel residues, which confirms their production from the CF mechanism. Indirect evidence of ICF was observed in the α - and p -emitting channels. Further, fission fragments' mass distribution is broad and symmetric, indicating their production through the compound nuclear mechanism. The variance of fission fragments' mass distribution shows an increasing trend with raising excitation energy.

DOI: [10.1103/PhysRevC.103.014608](https://doi.org/10.1103/PhysRevC.103.014608)

I. INTRODUCTION

Complete fusion (CF) of two massive nuclei leads to the formation of an excited compound nucleus (CN) that predominantly de-excites by evaporating particles or fission depending upon the available excitation energy and entrance channel parameters, like mass-asymmetry, angular momentum brought by the projectile. However, competition appears among the CF, pre-equilibrium (PEQ) process, and deep-inelastic collisions (DIC) in the low to intermediate energy range depending upon the entrance-channel mass-asymmetry. Apart from this, due to the low breakup threshold of weakly bound stable (^6Li , ^9Be , and $^{10,11}\text{B}$) and unstable halo nuclei (^{11}Li , ^{11}Be , and ^8B), some processes like incomplete fusion (ICF), elastic breakup, transfer followed by a breakup, emerge in the heavy-ion reaction dynamics [1]. Weakly bound projec-

tiles may break up before reaching the fusion barrier, leading to the suppression of CF at above barrier energies compared to one-dimensional barrier penetration model (1D-BPM) or coupled channels calculations [2,3]. It has been established from the experiments that CF, ICF, CF-fission (CFF), and ICF-fission (ICFF) are the dominating processes at energies around 10 MeV/nucleon [3–8]. An excited composite system decays through fission due to massive angular momentum transfer by the heavy-projectile to the target that lowers the fission barrier [9]; it yields an increment in fission cross sections.

Gasques *et al.* [3] reported that fission predominately originates from the completely fused compound nucleus rather than incomplete fusion in $^{10,11}\text{B} + ^{209}\text{Bi}$ reaction. Further, they suggested that a small contribution of fission following ICF could be understood in terms of excitation energy and angular momentum brought by the ICF fragment, which is, on average, lower than that of a complete projectile fusing to a target. However, Nishio *et al.* [10] demonstrated the evaporation residue cross sections, which are well approximated to the fission cross sections in $^{16}\text{O} + ^{238}\text{U}$ reaction at near to below barrier energies.

*Corresponding author: moumita.maiti@ph.iitr.ac.in

†Present address: Flerov Laboratory of Nuclear Reactions, Joint Institute for Nuclear Research, Dubna-141980, Russia.

Charge and mass yield distributions are fascinating post fission observables that have been extensively studied in the low and intermediate energy [4,11–17]. The proton-induced fission of ^{238}U [17] shows the asymmetric mass distribution at low excitation energy. However, asymmetry decreases as the excitation energy of composite system increases due to the washing of shell effects out. Besides this, symmetric and asymmetric mass and charge distributions of the fission fragments have been studied in heavy-ion reactions, such as $^{11}\text{B} + ^{181}\text{Ta}$ [4], $^{40}\text{Ar} + ^{238}\text{U}$ [5], $^{19}\text{F} + ^{169}\text{Tm}$ [6], $^{11}\text{B} + ^{232}\text{Th}$ [7], $^{16}\text{O} + ^{181}\text{Ta}$ [8], $^{12}\text{C} + ^{204}\text{Pb}$, $^{19}\text{F} + ^{197}\text{Au}$, and $^{30}\text{Si} + ^{186}\text{W}$ [11], $^{12}\text{C} + ^{232}\text{Th}$ [12], and $^{11}\text{B} + ^{238}\text{U}$ [14,15] and dispersion parameters have been extracted from many of these systems. Measured cross sections of the fission fragments from $^{11}\text{B} + ^{181}\text{Ta}$ reaction [4] at 125.7 MeV and 245.4 MeV show completely symmetric mass distribution. Earlier experiments [16,17] explained that the width of charge dispersion does not depend on the fissioning nuclei and excitation energy, and a small deviation in Gaussian fit of data was explained by the even-odd effect of the proton or neutron number. Moreover, they also emphasized that mass and charge variance [14], and mass and angular distribution [18] could be easily understood if the parameter, $Z^2/A \leq 37$, where Z and A are charge and mass of the fissioning nucleus. The elongated neck size explained the increased value of mass variance at the scission point for higher values of Z^2/A . In the similar direction, mass-energy and -angular distributions of fission fragments have been illustrated in $^{40,48}\text{Ca} + ^{144,154}\text{Sm}$ [19] and $^{11}\text{B} + ^{243}\text{Am}$ [20] reactions. Further, suppression in fusion cross sections and presence of quasifission were observed for deformed ^{154}Sm target at near and below barrier energies.

Apart from the fission fragments' mass and charge distribution, literature is also available on the CF-ICF and PEQ reaction mechanisms in low energy range [2,21–31]. Mukherjee *et al.* [23] studied the CF excitation functions for $^{10,11}\text{B} + ^{159}\text{Tb}$ and $^7\text{Li} + ^{159}\text{Tb}$ reactions at near barrier energies and estimated $\approx 84\%$ and $\approx 74\%$ suppression in CF for $^{10}\text{B} + ^{159}\text{Tb}$ and $^7\text{Li} + ^{159}\text{Tb}$ reactions, respectively. Similarly, suppression in CF cross-section was $\approx 15\%$ and $\approx 7\%$ for $^{10}\text{B} + ^{209}\text{Bi}$ and $^{11}\text{B} + ^{209}\text{Bi}$ reactions, respectively [3]. The observed suppression in CF could be due to the breakup of projectiles, and was correlated with the α -breakup threshold of weakly bound nuclei. Crippa *et al.* [25] also studied CF-ICF of $^{12}\text{C}(^8\text{Be} + \alpha)$ with ^{181}Ta target within ≈ 4 – 8 MeV/nucleon energy range. Besides this, heavy-ion reactions might also be useful to optimize the production of medically relevant radionuclides, such as ^{97}Ru (2.83 d), ^{101m}Rh (4.34 d), ^{103}Pd (16.99 d), and $^{207-210}\text{At}$ (1.63–8.1 h), ^{183}Os (13 h) via EQ and PEQ processes [32–38] and to validate the parameters used in the theoretical reaction codes.

The literature survey illustrates the lack of understanding of the heavy-ion-induced fusion-fission reaction dynamics in preactinide region. This article describes a study of the fusion-fission mechanism and the relative contribution of CF and ICF processes in $^{11}\text{B} + ^{181}\text{Ta}$ system within 53–63 MeV bombarding energy.

Descriptions of the experiment and model calculation have been presented in Secs. II and III, respectively. Section IV

sheds light on the data analysis and discussions, and finally, Sec. V concludes the article.

II. EXPERIMENTAL DETAILS

The experiment was performed using $^{11}\text{B}^{5+}$ beam delivered by the 14UD BARC-TIFR Pelletron facility, Mumbai, India. Self-supporting, pure (99.99%), thin natural Ta and Al foil targets having thicknesses 1.2–2.0 mg/cm² and 1.5–2.0 mg/cm², respectively, were prepared by proper rolling. Three target stacks were assembled, each of which contained two Ta-foils and two Al-foils alternatively. An Al-foil was placed behind each Ta-foil to catch the recoiled residues in the forward beam direction. Al-foil also helped in beam energy degradation to achieve a suitable energy separation between successive target foils. Each target stack was irradiated by ^{11}B beam, maintaining almost a constant beam current, and irradiation of three such target assembly was done by varying the incident beam energy, which dwelt between 53–63 MeV in the laboratory frame of reference. The average beam flux ($^{11}\text{B}^{5+}$) was $\approx 4 \times 10^{10}$ particles/sec during the experiment, and the average charge of ≈ 490 μC was collected for each irradiation. The total charge was measured by an electron-suppressed Faraday cup installed behind the target stack. The irradiation time, cooling time, and counting time were decided considering the evaporation residues' half-lives. Energy degradation of ^{11}B beam in each foil of a stack has been estimated using the SRIM (the stopping and range of the ions in the matter) code [39]. The projectile energy at a particular target is an average of the incident and outgoing energy. The average incident energies at the Ta-targets were 62.4 ± 0.7 , 59.6 ± 0.5 , 58.7 ± 0.8 , 56.6 ± 0.6 , 54.9 ± 0.8 , and 53.5 ± 0.6 MeV after the energy degradation in each target-catcher combination.

After the end of bombardment (EOB), residues trapped in the target-catcher foils were recorded using a large volume high purity germanium detector coupled with a PC-based multichannel analyzer (MCA) and GENIE-2K software for the γ -ray acquisition. The detector, which had energy resolution of 2.0 keV at 1332 keV γ -ray of ^{60}Co , was precalibrated using the conventional sources ^{137}Cs (30.08 y), ^{152}Eu (13.517 y), and ^{60}Co (5.27 y) of known activity. The populated products were identified by following their characteristic γ -rays and decay profile at each bombarding energy. The spectroscopic properties of the evaporation residues and fission-fragments are tabulated in Tables I and II. The unique characteristic γ -rays have been used to estimate the residues' cross-section at an incident energy E using the activation relation. A detailed description of the activity and cross-section measurement is available elsewhere in the literature [2,28]. The sources of uncertainty in cross-section are the following:

- (1) The uncertainty in determining the detector's geometry-dependent efficiency was $\leq 2\%$.
- (2) Error in the target thickness measurement was estimated as 2%.
- (3) Due to the fluctuation in beam current, the associated error in the incident beam flux was estimated as 6–7%.
- (4) Dead time of the detector was always kept $\leq 7\%$ by adjusting the geometry of measurement. The dead time

TABLE I. Nuclear spectroscopic data [53,54] of the populated residues via CF/ICF processes in $^{11}\text{B} + ^{181}\text{Ta}$ reaction.

Residue	J^π	$T_{1/2}$	Decay mode (%)	E_γ (keV)	I_γ (%)
^{189}Pt	$3/2^-$	10.87 h	$\epsilon^a + \beta^+$ (100)	113.82	2.5
				243.5	5.9
				568.85	6.0
^{188}Pt	0^+	10.2 d	$\epsilon + \beta^+$ (100), $\alpha(2.6 \times 10^{-5})$	195.05	18.4
				381.43	7.4
^{187}Pt	$3/2^-$	2.35 h	$\epsilon + \beta^+$ (100)	201.52	6.4
				304.71	4.3
				709.17	5.2
^{186}Pt	0^+	2.08 h	$\epsilon + \beta^+$ (100), $\alpha(1.4 \times 10^{-4})$	689.4	70.0
^{188}Ir	1^-	41.5 h	$\epsilon + \beta^+$ (100)	155.044	29.6
				478.0	14.7
				633.03	17.9
^{187}Ir	$3/2^+$	10.5 h	$\epsilon + \beta^+$ (100)	400.81	3.5
				427.02	3.7
				912.86	4.3
				977.54	2.8
^{186m}Ir	2^-	1.9 h	$\epsilon + \beta^+$ (75), IT^b (25)	137.14	23.0
				767.46	18.4
				773.24	11.7
^{186}Ir	5^+	16.64 h	$\epsilon + \beta^+$ (100)	434.84	33.9
^{183m}Os	$1/2^-$	9.9 h	$\epsilon + \beta^+$ (85), IT (15)	1101.94	49.0

^aElectron capture.^bIsomeric transition.

correction has been incorporated into the data. Statistical error in the background-subtracted peak area count, varying for each residue at each projectile energies, has been considered in the error calculation.

- (5) A finite error in the estimation of beam energy in the successive target-catcher foils was anticipated. However, energy straggling was assumed small [40,41].

The uncertainty associated with the incident projectile energy includes the error in SRIM calculation and target thickness determination. Reported error in cross-section and energy has been estimated by considering the factors mentioned above, and the measured data are reported in this article with 95% confidence.

III. THEORETICAL CALCULATIONS

The statistical model codes EMPIRE3.2.2 [42] and PACE4 [43] have been used to analyze the measured cross sections of the residues from the $^{11}\text{B} + ^{181}\text{Ta}$ reaction covering the incident energy range 53–63 MeV. Brief details of the models and input parameters chosen for the calculation to account for various reaction mechanisms have been described below.

EMPIRE was designed to comprehensively analyze reaction mechanisms involving both light and heavy ions as projectiles over a broad range of energy. It accounts for three main reaction mechanisms: direct reactions, pre-equilibrium

TABLE II. Nuclear spectroscopic data [53,54] of fission fragments populated in $^{11}\text{B} + ^{181}\text{Ta}$ reaction.

Radionuclide	$T_{1/2}$	E_γ (keV)	I_γ (%)
^{24}Na	14.997 h	1368.626	99.99
^{34m}Cl	32.0 min	146.36	38.30
^{66}Ge	2.26 h	536.74	6.2
^{74m}Br	46 min	1269.1	8.8
^{77}Kr	74.4 min	129.64	81.0
^{83}Br	2.374 h	529.589	1.3
^{87m}Sr	2.815 h	388.531	82.19
^{90}Mo	5.56 h	162.93	6.0
^{97m}Rh	46.2 min	189.21	48.5
^{103}Cd	7.3 min	1476.27	1.97
^{108}In	58 min	325.6	13.7
^{109}In	4.167 h	618.5	1.93
^{110m}In	69.1 min	657.75	97.74
^{115}Ag	20 min	1841.6	1.8
^{123}Xe	2.08 h	330.2	8.6
^{129}Sb	4.366 h	180.42	2.84
^{130}Sb	39.5 min	732	22.0
^{131}La	59 min	285.246	12.4
^{137}Nd	38.5 min	75.5, 505.1	17.3, 9.1
^{139m}Nd	5.5 h	796.5	4.2
^{149}Nd	1.728 h	198.928	1.39
^{160m}Ho	5.02 h	1408.2	36.0

(PEQ), equilibrium (EQ), or CN reaction. It has a provision of using quantum-mechanical PEQ models, such as multistep direct (MSD) and multistep compound (MSC) theory, and the phenomenological PEQ models, namely, exciton model (EM) and hybrid Monte Carlo simulation (HMS)-based DDHMS code, in its framework. However, a proper understanding of the quantum mechanical PEQ models for heavy ions is yet to come. The code has been used to estimate residual cross sections from the $^{11}\text{B} + ^{181}\text{Ta}$ reaction to analyze the measured data. In the present calculation, we have used the EM (PCROSS code) to estimate PEQ emissions and the Hauser-Feshbach (HF) formalism with width fluctuation correction (WFC) to account for the EQ cross sections of residues. The incorporation of WFC is necessary to establish a correlation between the incident and exit channels. However, WFC is essential only for a small number of open channels as EMPIRE automatically cutoff their calculations for excitation energies above around 10 MeV. Some details on these calculations are also available in literature [2,21,28]. To observe the effect of nuclear level density models in the residual cross sections, three phenomenological level density models: Gilbert-Cameron model (GC) [44], generalized super-fluid model (GSM) [45], and enhanced generalized superfluid model (EGSM) [46], with a mean free path parameter of 1.5 (optimum value), have been used to estimate the residual cross sections. Depending on the projectile type, EMPIRE considers an optical model for light-ion-induced fission while Sierk model [9] adequate for heavy-ion-induced fission.

PACE4 code, based on the Monte Carlo procedure, determines the decay sequence of an excited nucleus using the Hauser-Feshbach (HF) formalism of compound nuclear

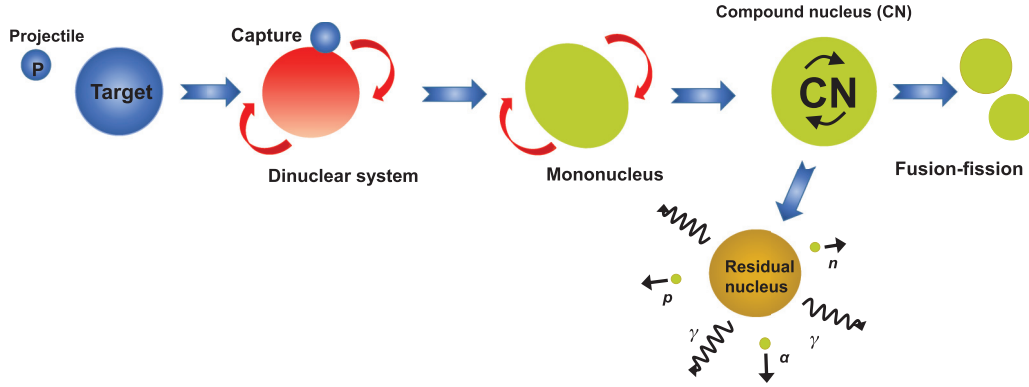


FIG. 1. A pictorial representation of the formation of an excited compound nucleus that predominantly de-excites by particle evaporation or fission.

reaction. Monte Carlo procedure provides a correlation between the emitted particles, γ rays, and energy and angular distributions of particles. The random number selection helps determine the actual final state to which the nucleus decays, and this process is repeated for the other cascades until all the nuclei reach the ground state. The code incorporates the angular momentum projections at each stage of the de-excitation to predict the angular momentum distribution of emitted particles. The fusion cross-section is estimated using the Bass model [47]. The transmission coefficients of evaporated light particles, such as n , p , and α , are determined from the optical model, whose parameters are taken from Ref. [48].

The cross sections of residues produced from the $^{11}\text{B} + ^{181}\text{Ta}$ reaction have been estimated using the code. The level density parameter (a), used in this model, is defined as $a = A/K$, where A is the mass number of the compound nucleus, and K is a free parameter known as level density parameter constant. In the present analysis, we have used $K = 8, 9$, and 10 . In PACE4, fission is considered a decay mode of CN and is calculated using a modified rotating liquid drop fission barrier by Sierk [9]. The a ratio, a_f/a_n (where a_f and a_n are the level-density parameters for fission and neutron emissions, respectively) is taken as unity. It may be noted that the PACE4 code does not consider PEQ phenomena, ICF, or transfer mechanisms.

IV. DATA ANALYSIS AND DISCUSSIONS

The ^{11}B -induced reactions in ^{181}Ta led to the formation of $^{186,187,188,189}\text{Pt}$, $^{186m,186,187,188}\text{Ir}$, and ^{183m}Os radionuclides via CF and ICF processes. Besides, experimental data analysis ensured the production of other residues unexpected from the CF or ICF mechanisms. These residues have charge and atomic mass values around half of those produced by CF and ICF processes, indicating the possibility of their production through the fission of compound nucleus formed via CF and ICF processes in $^{11}\text{B} + ^{181}\text{Ta}$ reaction. A pictorial representation of CN evaporation and fission mode has been shown in Fig. 1. The fission fragments populated within the energy range considered are ^{24}Na , ^{34m}Cl , ^{66}Ge , $^{74m,83}\text{Br}$, ^{77}Kr , ^{87m}Sr , ^{90}Mo , ^{97m}Rh , ^{103}Cd , $^{108,109,110m}\text{In}$, ^{115}Ag , ^{123}Xe , $^{129,130}\text{Sb}$, ^{131}La , $^{137,139m,149}\text{Nd}$, and ^{160m}Ho . A typical γ -ray spectrum

of the 62.4 MeV ^{11}B -irradiated ^{181}Ta , collected after 30 min of the EOB, is shown in Fig. 2, where residues are marked corresponding to their characteristic γ -peaks. The dead-time corrected and background-subtracted peak area of unique γ -rays of each residue was analyzed to estimate the residual activity, and the corresponding cross sections were calculated using the activation relation [2,28].

A. Residual cross-sections

Measured cross sections of the residues populated by CF and ICF, tabulated in Table III, are compared with the theory as presented in Figs. 3 and 4. Symbols with uncertainty represent measured data, while lines present theoretical predictions. Analysis of the residual excitation functions and other derived results are presented in the following sections as a function of center-of-mass energy ($E_{\text{c.m.}}$).

In general, PACE and EMPIRE reproduce the measured excitation function of $^{186,187,188,189}\text{Pt}$ grossly, as can be seen from Fig. 3. The trend of the measured cross sections of ^{189}Pt [Fig. 3(a)], produced through $^{181}\text{Ta}(^{11}\text{B}, 3n)$ reaction, is reproduced by EMPIRE predictions, which used HF for EQ, EM for PEQ process, and three different level density models: EGSM, GSM, and GC, throughout the energy range. Simultaneously, PACE with $K = 8$ and 9 underestimates the measured data, while PACE with $K = 10$ satisfies at the two lower energies, 50.4 and 51.8 MeV. EMPIRE level densities (EGSM and GC) are very close to each other ≤ 52 MeV, beyond which they start diverging and reproduce the measured data at three higher energy points. On the other side, predictions from EMPIRE with GSM is ≈ 58 –22% lower than the other two level density models (EGSM and GC), and GSM level density model predictions are very close to the experimental data throughout the energy range. Hence, one can conclude that the excitation function of ^{189}Pt (mainly $3n$ -channel) resulted from the PEQ and EQ neutrons. It has now been established that PEQ nucleons have slightly higher energy than those emitted from the fully equilibrated nucleons. Thus, an admixture of PEQ with EQ processes is necessary for the best reproduction of the experimental data. Emission of PEQ neutrons in case of $3n$ channel residues was also observed in other heavy-ion-induced reactions [21,31,34]. A

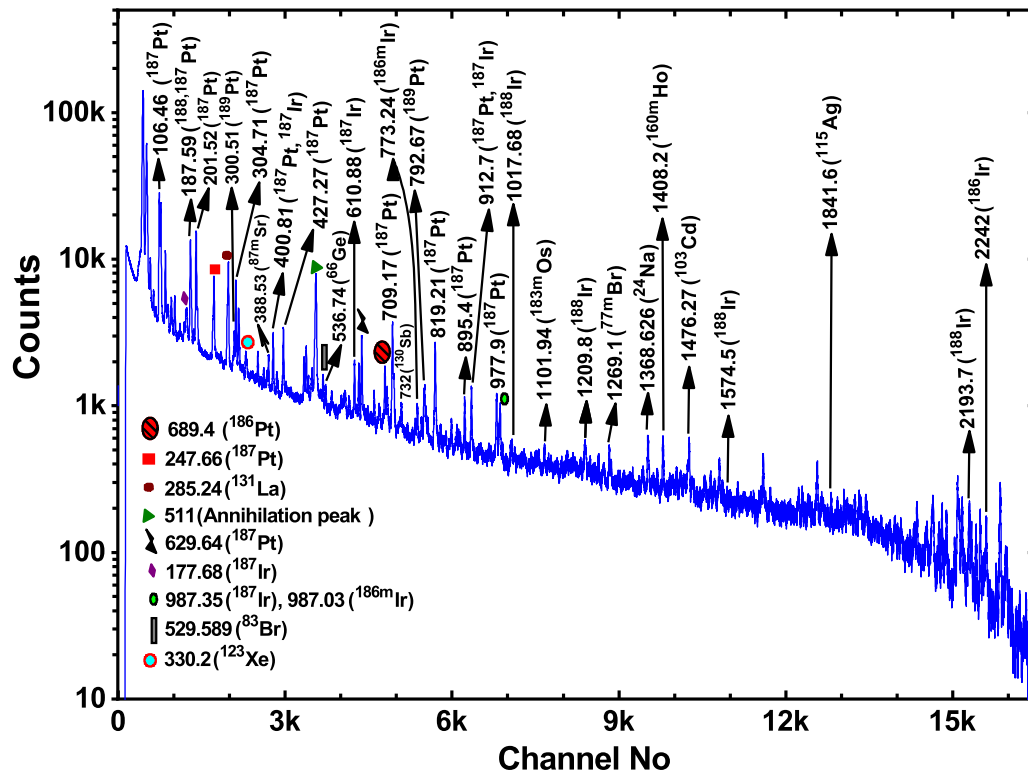


FIG. 2. A typical γ -ray spectrum of the $E_{\text{lab}} = 62.4$ MeV ^{11}B irradiated ^{181}Ta collected 30 min after the EOB. The energy of the γ -ray peaks are in keV.

critical observation shows that PACE with $a = A/10$ offers the best result; therefore, PACE with $a = A/10$ has been used to analyze other fellow residues.

The measured cross sections of $^{181}\text{Ta}(^{11}\text{B}, 4n)^{188}\text{Pt}$ are compared with the theoretical excitation function estimated from PACE and EMPIRE as presented in Fig. 3(b). One can notice that the theoretical cross sections from PACE with $K = 10$ are successfully reproducing the measured data throughout the energy range, while predictions from EMPIRE with EGSM and GC level density models reasonably agree with the measured data except at 58.8 MeV energy. However, EMPIRE with GSM underestimates the measured data throughout the energy range. The measured data of ^{187}Pt is satisfactorily explained by PACE above 54 MeV [Fig. 3(c)], below which it underpredicts the data. However, EMPIRE with the GC model explains the measured data quite well throughout the energy range except for 50.4 and 53.4 MeV energy, while two other level density models, EGSM and GSM, underpredict the measured data over the entire range of energy. Thus, it can be concluded that the production of ^{188}Pt and ^{187}Pt is purely through the CN reaction mechanism. Figure 3(c) also shows a comparison between the measured cross sections of $^{181}\text{Ta}(^{11}\text{B}, 6n)^{186}\text{Pt}$ at $E_{\text{c.m.}} = 58.8$ and 56.2 MeV and theoretical predictions. One can notice that the theoretical estimations from EMPIRE with GC model could successfully explain the measured data while other models (EGSM and GSM) underpredict them. Similarly, predictions from PACE with $K = 10$ are lower than the measured data.

The sum of cross sections measured for xn -channel residues, i.e., $^{186,187,188,189}\text{Pt}$, have been compared with those

predicted from EMPIRE with EGSM, GSM, and GC models, and PACE with $K = 10$, as shown in Fig. 3(d). One can observe that EMPIRE with EGSM and GC, and PACE reasonably reproduce the measured data while EMPIRE with GSM falls apart. However, EMPIRE with GC model and PACE with $K = 10$ estimations reproduce the measured data more accurately. Therefore, we have implemented theoretical predictions with those options to compare pxn and αxn channels, shown in Fig. 4.

Experimentally measured cross sections of Ir and Os isotopes have been compared with the theoretical estimations from EMPIRE and PACE codes based on the EQ and PEQ models, as shown in Fig. 4. In general, the trend of theoretical excitation functions is similar to that of the measured data. Figure 4(a) shows the measured cross section of ^{188}Ir as a function of projectile energy. Theoretical cross sections of ^{188}Ir , resulted from $p3n$ channel, estimated from EMPIRE with GC and PACE, are close to each other at energy ≈ 55 MeV, but underpredict the data throughout the energy range. A comparison of ^{187}Ir is presented in Fig. 4(b). The measured cross sections of ^{187}Ir are significantly large compared to the $p4n$ channel predictions of EMPIRE and PACE. This is because the residues have been produced through two reaction paths, (i) direct channel $^{181}\text{Ta}(^{11}\text{B}, p4n)^{187}\text{Ir}$ and (ii) indirectly through the decay of its precursor $^{181}\text{Ta}(^{11}\text{B}, 5n)^{187}\text{Pt} \rightarrow ^{187}\text{Ir}$, and the measured ^{187}Ir cross sections are cumulative. Hence, we have compared measured ^{187}Ir cross sections with the sum of ^{187}Pt and ^{187}Ir cross sections obtained from EMPIRE and PACE as presented in Fig. 4(b). Although the difference between theory and experiment has been

TABLE III. Production cross section of evaporation residues and fission fragments at various incident energies.

Residues (\downarrow)	Cross section (mb)					
	$E_{\text{lab}} = 62.4 \pm 0.7$ MeV	59.6 ± 0.5 MeV	58.7 ± 0.8 MeV	56.6 ± 0.6 MeV	54.9 ± 0.8 MeV	53.5 ± 0.6 MeV
	$E_{\text{c.m.}} = 58.8 \pm 0.7$ MeV	56.2 ± 0.5 MeV	55.4 ± 0.7 MeV	53.4 ± 0.5 MeV	51.8 ± 0.8 MeV	50.4 ± 0.5 MeV
^{24}Na	18.3 ± 2.2	15.0 ± 2.0	26.0 ± 2.7	23.0 ± 2.8	18.0 ± 1.9	22.2 ± 2.6
^{34m}Cl	18.5 ± 2.6	12.1 ± 1.7	27.2 ± 2.2	96.7 ± 10.4	79.7 ± 8.5	96.4 ± 11.5
^{66}Ge	38.7 ± 5.6	24.8 ± 4.5	21.6 ± 3.3	10.8 ± 2.4	2.8 ± 0.8	2.2 ± 0.9
^{74m}Br	29.0 ± 4.8	25.6 ± 5.1	26.5 ± 4.6	11.1 ± 3.1	–	–
^{77}Kr	3.61 ± 0.50	0.15 ± 0.07	1.98 ± 0.29	0.22 ± 0.07	0.40 ± 0.09	0.11 ± 0.05
^{83}Br	232.8 ± 32.3	118.4 ± 19.6	111.6 ± 12.6	56.5 ± 11.7	12.9 ± 4.6	9.5 ± 4.8
^{87m}Sr	3.62 ± 0.46	1.82 ± 0.30	1.55 ± 0.27	1.08 ± 0.14	0.25 ± 0.07	0.29 ± 0.10
^{90}Mo	5.4 ± 1.6	9.7 ± 2.2	3.9 ± 1.3	2.3 ± 1.1	0.9 ± 0.5	1.3 ± 0.9
^{97m}Rh	–	3.09 ± 0.59	–	2.03 ± 0.38	–	0.50 ± 0.19
^{108}In	–	0.77 ± 0.40	–	–	–	–
^{109}In	29.3 ± 8.5	30.8 ± 8.2	14.1 ± 5.1	20.0 ± 6.0	7.1 ± 2.4	–
^{110m}In	–	0.15 ± 0.08	–	–	–	–
^{123}Xe	18.8 ± 2.7	14.7 ± 2.4	6.9 ± 1.4	5.1 ± 1.3	0.6 ± 0.3	1.1 ± 0.7
^{129}Sb	3.8 ± 2.0	13.2 ± 3.6	2.1 ± 1.1	5.8 ± 2.2	1.1 ± 0.6	3.2 ± 1.8
^{130}Sb	15.1 ± 2.3	11.8 ± 2.0	9.1 ± 2.1	5.6 ± 1.2	1.17 ± 0.64	1.56 ± 0.75
^{131}La	121.5 ± 12.7	115.2 ± 12.4	104.2 ± 11.2	62.2 ± 7.2	14.8 ± 2.0	13.5 ± 2.2
^{137}Nd	–	9.2 ± 2.0	–	9.2 ± 2.2	–	8.2 ± 1.5
^{139m}Nd	31.3 ± 5.8	45.2 ± 8.2	11.1 ± 3.1	20.6 ± 4.8	2.2 ± 1.0	4.7 ± 2.1
^{149}Nd	–	33.6 ± 7.0	–	15.7 ± 4.8	–	–
^{160m}Ho	20.1 ± 2.5	9.2 ± 1.6	11.1 ± 1.5	4.6 ± 1.0	2.2 ± 0.4	1.7 ± 0.5
^{189}Pt (3n)	9.9 ± 3.6	13.9 ± 4.1	14.2 ± 2.9	18.1 ± 3.8	16.9 ± 2.8	21.5 ± 4.4
^{188}Pt (4n)	288.1 ± 35.4	404.8 ± 57.8	500.5 ± 62.6	450.3 ± 60.0	415.2 ± 50.3	372.0 ± 46.4
^{187}Pt (5n)	440.8 ± 45.0	270.9 ± 30.0	216.2 ± 22.4	110.3 ± 13.1	31.3 ± 3.8	21.5 ± 3.5
^{186}Pt (6n)	8.5 ± 1.0	0.35 ± 0.14	–	–	–	–
^{188}Ir (p3n)	52.3 ± 7.4	35.4 ± 5.0	37.5 ± 5.1	25.3 ± 4.0	25.2 ± 3.4	20.6 ± 3.4
^{187}Ir (Cum)	730.4 ± 90.5	369.2 ± 42.3	347.3 ± 38.4	156.6 ± 20.3	59.5 ± 8.9	33.8 ± 6.5
^{186m}Ir (p5n)	23.3 ± 3.0	14.3 ± 2.8	10.7 ± 1.9	4.1 ± 1.1	2.2 ± 0.5	–
^{186}Ir (p5n)	7.0 ± 1.6	1.7 ± 0.5	1.3 ± 0.6	–	–	–
^{183m}Os (α 5n)	6.8 ± 1.3	2.3 ± 0.8	2.4 ± 0.6	1.3 ± 0.4	–	–

reduced, cross sections are still larger than those expected from the models.

The measured production cross sections of $^{186m,186}\text{Ir}$, $^{186(m+g)}\text{Ir}$ are presented in Fig. 4(c), and those for ^{183m}Os are plotted in Fig. 4(d) and compared with the theoretical cross section of $^{181}\text{Ta}(^{11}\text{B}, p5n)^{186(m+g)}\text{Ir}$ and $^{181}\text{Ta}(^{11}\text{B}, \alpha 5n)^{183m}\text{Os}$ obtained from EMPIRE, respectively. EMPIRE grossly underestimates both the isotopes. Although absolute values of measured cross sections are small, they are much larger than the EMPIRE predictions. Since production of ^{186}Pt has been identified at $E_{\text{c.m.}} = 58.8$ MeV and 56.2 MeV, measured cross sections of ^{186}Ir are expected to be cumulative above $E_{\text{c.m.}} = 56.2$ MeV. ^{186}Ir was possibly populated by two different routes (i) direct channel $^{181}\text{Ta}(^{11}\text{B}, p5n)^{186}\text{Ir}$ and (ii) indirectly through the decay of its precursor, $^{181}\text{Ta}(^{11}\text{B}, 6n)^{186}\text{Pt} \rightarrow ^{186}\text{Ir}$, although contribution is tiny in this case. Therefore, Fig. 4(c) also compares ^{186}Ir data with the sum of ^{186}Pt and $^{186}\text{Ir}(m+g)$ cross sections obtained from EMPIRE, measured cross sections are still large compared to the model predictions. PACE did not show the production of $^{186m,186g}\text{Ir}$, and ^{183m}Os within the energy range considered.

It is worth mentioning that the theoretical cross sections for EMPIRE with GSM in xn and pxn channels are significantly

low compared to the two other models, EGSM and GC. It has been observed that the cross sections in some other α channels, which are not produced experimentally, are significantly high in the case of GSM, and that conserves the total fusion cross section.

In general, the measured cross section of Ir and Os isotopes have enhanced cross sections over the energy range compared to the theoretical estimations from EMPIRE and PACE, whereas the models satisfactorily reproduced the xn -channel residues. It is, thus, assumed that Ir and Os isotopes might have been produced from both CF and ICF channel, while the theoretical models consider only the complete fusion of ^{11}B in ^{181}Ta ; as a result, the difference between them is observed. Hence, the enhanced cross section over the EMPIRE prediction is attributed to the ICF of ^{11}B . Our observation is in corroboration with the study reported by Gasques *et al.* due to the breakup of ^{11}B [3].

The direct production route of Ir and Os isotopes is through the pxn and αxn channels, respectively, in competition with xn channel and fission after CF of ^{11}B . Since CF is not the only mechanism for the production of Ir and Os isotopes, ICF of ^{11}B be explored to understand their productions. ^{11}B may break up into fragments before fusing to the target nuclei, the

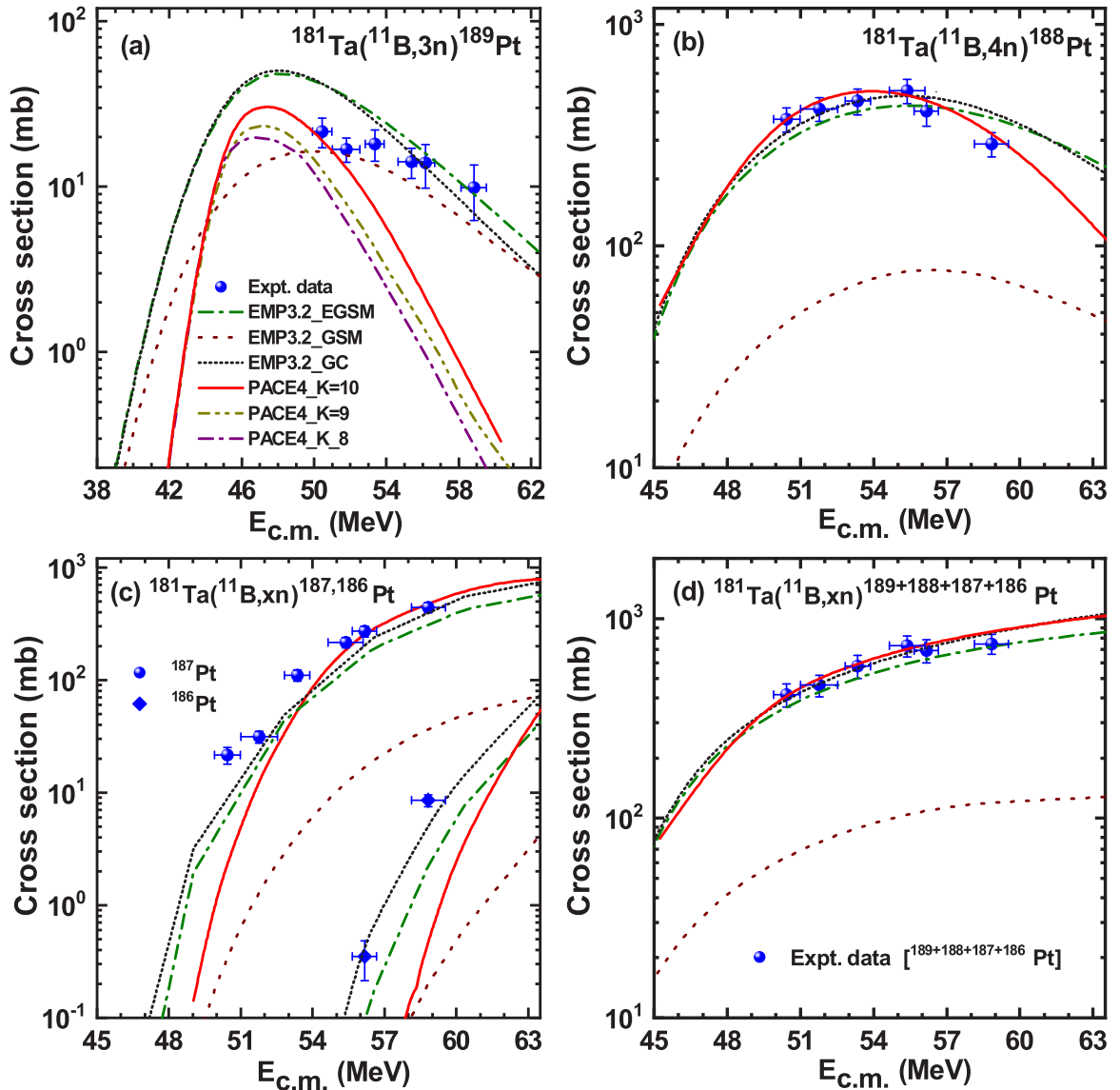


FIG. 3. Comparison between measured excitation function of (a) ^{189}Pt , (b) ^{188}Pt , (c) $^{187,186}\text{Pt}$, and (d) $^{186+187+188+189}\text{Pt}$ with the theoretical predictions of EMPIRE3.2.2 (denoted by EMP3.2) and PACE4.

possible breakup processes of ^{11}B are as follow [Eq. (1)]:

$$\begin{aligned}
 ^{11}\text{B} &\rightarrow ^7\text{Li} + \alpha, \quad Q = -8.664 \text{ MeV}, \\
 ^{11}\text{B} &\rightarrow ^8\text{Be} + ^3\text{H}, \quad Q = -11.224 \text{ MeV}, \\
 &\rightarrow \alpha + \alpha + ^3\text{H}, \quad Q = -11.132 \text{ MeV}. \quad (1)
 \end{aligned}$$

Although the favorable breakup channel of ^{11}B appears to be $^7\text{Li} + \alpha$ due to the low Q value, both are possible when the projectile carry considerably large energy.

- (1) CF: complete fusion of ^{11}B in ^{181}Ta leads to the formation of a compound nucleus $^{192}\text{Pt}^*$ in the excited state which de-excites through the emission of light particles (e.g., n , p , α , etc.) and produce residual nuclei $^{189,188,187,186}\text{Pt}$, $^{188,187,186}\text{Ir}$, and ^{183m}Os as listed in Table. IV.

- (2) ICF: ^{11}B may break up into its cluster fragments [Eq. (1)], and if one of the fragments fuses with the target nucleus, forming a reduced CN, and the other may fly away in the forward direction as a spectator. The following ICF processes could be responsible for the enhanced production of ^{186}Ir , ^{187}Ir , ^{188}Ir , and ^{183m}Os in the $^{11}\text{B} + ^{181}\text{Ta}$ reaction (see Table IV).

- (a) The fusion of ^7Li particle, a direct breakup component of ^{11}B , in ^{181}Ta leads to the formation of excited compound nucleus $^{188}\text{Os}^*$, which may produce ^{183m}Os by emitting five neutrons, and α particle moves with the proportionate velocity as a spectator.
- (b) ^{11}B may break into ^8Be and t [Eq. (1)], and fusion of ^8Be in ^{181}Ta could lead to the formation of $^{189}\text{Ir}^*$, which may emit neutrons and protons to

TABLE IV. CF and ICF reaction channels and corresponding Q values.

CF of ^{11}B		ICF of ^{11}B ($^{11}\text{B} \rightarrow ^7\text{Li} + \alpha$ or $^8\text{Be} + ^3\text{H}$)	
Reaction	Q value (MeV)	Reaction	Q value (MeV)
$^{181}\text{Ta}(^{11}\text{B}, 3n)^{189}\text{Pt}$	-27.5	$^{181}\text{Ta}(^7\text{Li}, 5n)^{183\text{m}}\text{Os}$	-30.2
$^{181}\text{Ta}(^{11}\text{B}, 4n)^{188}\text{Pt}$	-34.2	$^{181}\text{Ta}(^8\text{Be}, n)^{188}\text{Ir}$	-13.2
$^{181}\text{Ta}(^{11}\text{B}, 5n)^{187}\text{Pt}$	-43.4	$^{181}\text{Ta}(^8\text{Be}, 2n)^{187}\text{Ir}$	-20.1
$^{181}\text{Ta}(^{11}\text{B}, 6n)^{186}\text{Pt}$	-50.3	$^{181}\text{Ta}(^8\text{Be}, 3n)^{186}\text{Ir}$	-28.5
$^{181}\text{Ta}(^{11}\text{B}, p3n)^{188}\text{Ir}$	-32.9	$^{181}\text{Ta}(^8\text{Be}, p5n)^{183\text{m}}\text{Os}$	-47.5
$^{181}\text{Ta}(^{11}\text{B}, p4n)^{187}\text{Ir}$	-39.8		
$^{181}\text{Ta}(^{11}\text{B}, p5n)^{186}\text{Ir}$	-48.2		
$^{181}\text{Ta}(^{11}\text{B}, \alpha 5n)^{183\text{m}}\text{Os}$	-38.9		

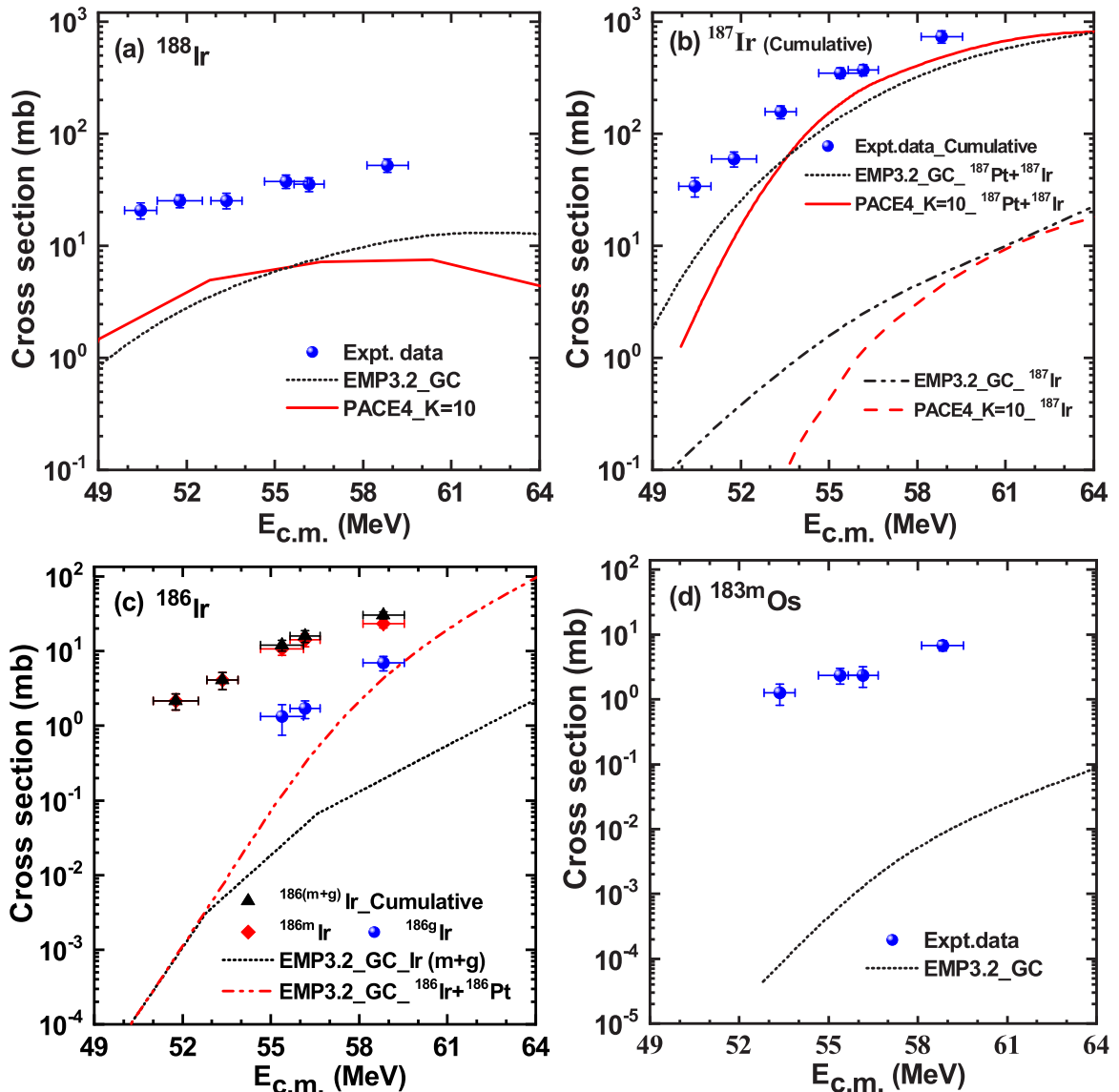


FIG. 4. Comparison between measured excitation function of (a) ^{188}Ir , (b) ^{187}Ir (Cumulative), (c) $^{186}\text{Ir}(m+g)$ (Cumulative), and (d) $^{183\text{m}}\text{Os}$ with the theoretical predictions.

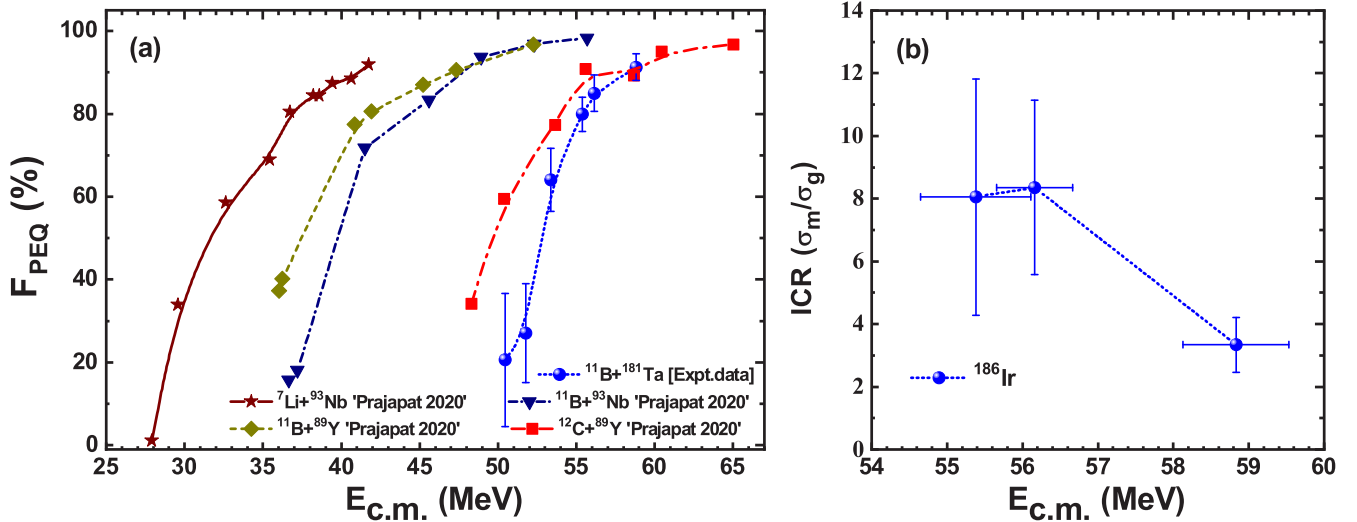


FIG. 5. (a) Variation of F_{PEQ} as a function of $E_{\text{c.m.}}$ for $^{11}\text{B} + ^{181}\text{Ta}$ (Present work) and $^{7}\text{Li} + ^{93}\text{Nb}$, $^{11}\text{B} + ^{89}\text{Y}$, $^{11}\text{B} + ^{93}\text{Nb}$, $^{12}\text{C} + ^{89}\text{Y}$; Prajapat 2020 [31] systems, (b) Variation of ICR of ^{186}Ir with $E_{\text{c.m.}}$.

produce the measured isotopes of Ir and Os, when t moves as a spectator.

- (c) ^{11}B may also break into two α -particles and t [Eq. (1)]. However, the fusion of α in ^{181}Ta would not lead to the production of Ir and Os isotopes.

ICF's contribution to the production of pxn and αxn channel residues has been analyzed by taking the EMPIRE's estimation with a GC-level density model as a reference. It confirms that the production of $^{186(m+g)}\text{Ir}$ and ^{183m}Os is purely through the ICF process as the EMPIRE's estimation for them is negligibly small, and PACE shows no possibility of their production. The contribution of ICF ($\sigma_{\text{ICF}} = \sigma_{\text{Res}}^{\text{Expt}} - \sigma_{\text{Res}}^{\text{EMP}}$) to the measured ^{188}Ir and ^{187}Ir is more than 80% and 90%, respectively, over the energy range considered. However, the strength of ICF, which increases with energy, for the measured pxn and αxn channels lies between 5–20% for the $^{11}\text{B} + ^{181}\text{Ta}$ reaction up to $E_{\text{c.m.}} = 58.8$ MeV.

B. PEQ fraction and isomeric cross section ratio

It is evident from Fig. 3(a) that theoretical predictions from PACE with $K = 10$, which considers only EQ emissions in the framework of the HF model, underestimate the measured data of $^{181}\text{Ta}(^{11}\text{B}, 3n)^{189}\text{Pt}$ toward the high-energy tail of the excitation function, while satisfactorily reproduced the data at two lower-energy points. The difference observed between the measured data and pure EQ emission estimated from PACE could be attributed to the PEQ emission of a few neutrons. In support of this, a combination of EQ and PEQ models (HF+EM) used in EMPIRE could reproduce the measured data. We have calculated the strength of the PEQ fraction, defined as F_{PEQ} (in %) = $(\sigma_{\text{EQ+PEQ}}^{\text{expt}} - \sigma_{\text{EQ}}^{\text{th}}) \times 100 / (\sigma_{\text{EQ+PEQ}}^{\text{expt}})$, where $\sigma_{\text{EQ+PEQ}}^{\text{expt}}$ is the measured cross-section of a residue populated by EQ and PEQ processes, $\sigma_{\text{EQ}}^{\text{th}}$ corresponds to the EQ cross-section of the residue calculated theoretically using PACE. It can be observed from Fig. 5(a) that the PEQ fraction is increasing with increasing energy. The estimated PEQ

cross sections ($\sigma_{\text{EQ+PEQ}}^{\text{expt}} - \sigma_{\text{EQ}}^{\text{th}}$) of ^{189}Pt contributes ≈ 5 –20% to integral PEQ cross-section, and the total theoretical PEQ cross-section is ≈ 8 –15% of the total reaction cross section for this reaction within the studied energy range.

Further, we have compared the F_{PEQ} of $^{11}\text{B} + ^{181}\text{Ta}$ reaction with the $^{7}\text{Li} + ^{93}\text{Nb}$, $^{11}\text{B} + ^{89}\text{Y}$, $^{11}\text{B} + ^{93}\text{Nb}$, and $^{12}\text{C} + ^{89}\text{Y}$ reactions [31] studied earlier. It is worth mentioning here that the PEQ fraction threshold is different for each reaction, PEQ starts from ≈ 28 , 36, 38, 50, and 52 MeV for $^{7}\text{Li} + ^{93}\text{Nb}$, $^{11}\text{B} + ^{89}\text{Y}$, $^{11}\text{B} + ^{93}\text{Nb}$, $^{12}\text{C} + ^{89}\text{Y}$, and $^{11}\text{B} + ^{181}\text{Ta}$ reactions, respectively, which mainly due to the variation in Coulomb barrier between the two heavy colliding partners.

A nucleus having ground and isomeric states with measurable half-lives is used to estimate the isomeric cross-section ratio (ICR), which yields an understanding of γ de-excitation processes, conversion of angular momentum, and couplings of different reaction channels. To understand ICR's dependency on factors like relative spins of the ground and isomeric states, projectile energy, types of emitted particles, level difference, and compound nucleus decay, ICR has been estimated for $^{186,186m}\text{Ir}$ pair. In present study, ICR has been defined as the ratio of cross sections of isomeric state (σ_m) to ground-state (σ_g), $\text{ICR} = \sigma_m/\sigma_g$. The ^{186}Ir and ^{186m}Ir have ground state spin 5^+ and 2^- at 0.0 and 0.0 keV energies, respectively. The measured ICR value increases at the beginning due to the population of the low spin state (2^-) while it decreases beyond 56 MeV, as shown in Fig. 5(b). However, as the excitation energy of the compound nucleus increases, the population of the higher spin state (5^+), i.e., the ground state of ^{186}Ir increases. Reports on the similar ICR trend could be found in the literature [2,34].

C. Isotopic and isobaric yield distributions of Nd and In isotopes

Measuring isotopic yields of fission-fragments is complicated because of the need for accurate branching ratios

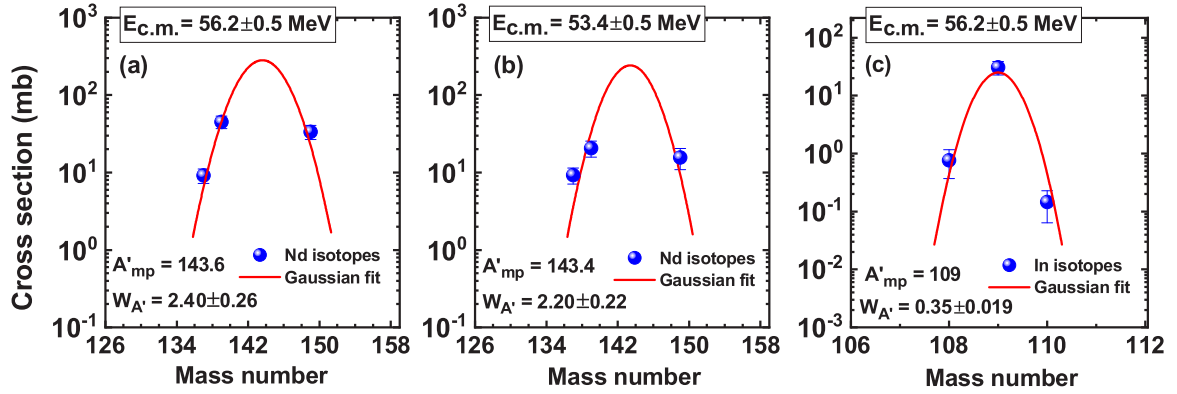


FIG. 6. Isotopic yield distribution for ($^{137,139m,149}\text{Nd}$) neodymium isotopes at (a) $E_{c.m.} = 56.2$ MeV, (b) $E_{c.m.} = 53.4$ MeV, and for (c) indium isotopes ($^{108,109,110m}\text{In}$) at $E_{c.m.} = 56.2$ MeV. Red line represents the Gaussian fit.

[49]. After its formation, the excited CN predominantly de-excites by evaporating particles or fission depending upon the available excitation energy and other entrance channel parameters. Moreover, heavier charged particle emission may be hindered due to the large Coulomb barrier. Hence, nucleon (proton/neutron) emissions from the fission fragments may give rise to the isotopic and isobaric yield distributions. The isotopic and isobaric yield distribution of neodymium ($^{137,139m,149}\text{Nd}$) and indium ($^{108,109,110m}\text{In}$) isotopes have been analyzed from the measured cross sections, shown in Figs. 6 and 7. For the prediction of total mass chain yield of a fission product of mass A , charge Z , the knowledge of the most probable mass and width parameter of mass distribution is essential. It is well established that the independent isotopic yield of any product could be described by the Gaussian distribution

$$Y(A, Z) = \frac{Y_Z}{\sqrt{2\pi W_{A'}^2}} e^{-0.5(A-A'_{mp})^2/W_{A'}^2}, \quad (2)$$

where A'_{mp} is the most probable mass, $W_{A'}$ is the width parameter of the isotopic yield distribution obtained from Gaussian distribution, and Y_Z is the chain yield of isotopes.

The χ^2 minimization was carried out using a nonlinear least-square curve fit method during the Gaussing fitting of data. The dispersion parameters (A'_{mp} and $W_{A'}^2$) were obtained from the experimentally measured independent yield of Nd and In isotopes, as shown in Figs. 6(a)–6(c). The most probable mass (A'_{mp}) of Nd and In isotopes at $E_{c.m.} = 56.2$ MeV are found to be 143.6 and 109, respectively. The width parameter ($W_{A'}$) for Nd and In isotopes at $E_{c.m.} = 56.2$ MeV are predicted to be 2.4 ± 0.26 and 0.35 ± 0.019 , respectively. The A'_{mp} and $W_{A'}$ values obtained by fitting Nd isotopes measured at a lower energy (53.4 MeV) [Fig. 6(b)] are found consistent with those extracted at 56.2 MeV. Further, the variance ($W_{A'}^2$) of isotopic yield distribution obtained from the Gaussian fit of Nd and In isotopes have been listed in Table V and are found to be in good agreement for Nd isotopes with the literature values of the similar systems while it is less for In isotopes.

In low energy complete fusion-fission reactions, the charge distribution of two complementary fission fragments provides the evolutionary idea of those fragments' nuclear charge distributions. As it is mandatory to have information of the most probable charge (Z_{mp}) and width parameter (W_Z) of the charge distribution, collectively known as dispersion parameters (Z_{mp}

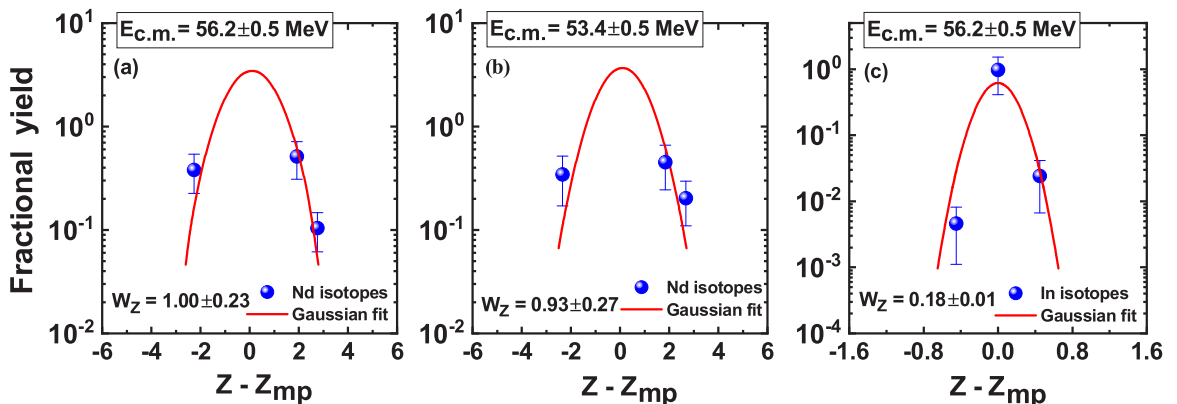


FIG. 7. Fractional yield (FY) distribution for neodymium isotopes ($^{137,139m,149}\text{Nd}$) as a function of corrected charge ($Z - Z_{mp}$) at (a) $E_{c.m.} = 56.2$ MeV, (b) $E_{c.m.} = 53.4$ MeV, and for (c) indium isotopes ($^{108,109,110m}\text{In}$) at $E_{c.m.} = 56.2$ MeV. Red line represents the Gaussian fit.

TABLE V. Comparison of variance (W_A^2) of isotopic yield distribution for different fissioning systems.

Reaction	E^* (MeV)	Fragment	W_A^2	References
$^{11}\text{B} + ^{181}\text{Ta}$	52.7	Nd	5.76 ± 0.52	Present work
$^{11}\text{B} + ^{181}\text{Ta}$	49.9	Nd	4.84 ± 0.44	Present work
$^{11}\text{B} + ^{181}\text{Ta}$	52.7	In	0.12 ± 0.038	Present work
$^{11}\text{B} + ^{232}\text{Th}$	55.68	Sb	4.0	[7]
$^{11}\text{B} + ^{232}\text{Th}$	55.68	I	5.43	[7]
$^{11}\text{B} + ^{232}\text{Th}$	55.68	Cs	3.72	[7]
$^{11}\text{B} + ^{238}\text{U}$	67.5	Rb	3.84 ± 0.16	[15]
$^{11}\text{B} + ^{238}\text{U}$	67.5	Cs	3.95 ± 0.14	[15]
$^{22}\text{Ne} + ^{238}\text{U}$	64.5	Rb	4.23 ± 0.40	[15]
$^{22}\text{Ne} + ^{238}\text{U}$	64.5	Cs	4.26 ± 0.90	[15]
$^{19}\text{F} + ^{169}\text{Tm}$	71.2	Nd	5.19 ± 0.56	[6]
$^{19}\text{F} + ^{169}\text{Tm}$	71.2	In	4.97 ± 1.30	[6]
$^{19}\text{F} + ^{169}\text{Tm}$	69.4	Nd	4.92 ± 0.80	[6]
$^{19}\text{F} + ^{169}\text{Tm}$	69.4	In	4.49 ± 1.10	[6]
$^{19}\text{F} + ^{169}\text{Tm}$	58.5	Nd	4.24 ± 0.22	[6]
$^{19}\text{F} + ^{169}\text{Tm}$	58.5	In	3.96 ± 1.0	[6]
$^{16}\text{O} + ^{181}\text{Ta}$	67.04	Y	3.05 ± 0.10	[8]
$^{16}\text{O} + ^{181}\text{Ta}$	67.04	In	4.16 ± 0.01	[8]

and W_Z), for the isobaric mass chain of fission products having mass A and charge Z to deduce the total chain yield [7]. According to the unchanged charge densities (UCD) hypothesis [50], the most probable charge Z_{mp} for Nd and In isotopes was deduced using the following formula

$$Z_{\text{mp}}(A) = \left(\frac{Z}{A'} \right) A \quad (3)$$

The fractional yields [FY(Z)] of Nd and In isotopes were calculated by dividing the independent yields of isotopes by the corresponding charge (Z) yield to which a particular isotope belongs. The corrected isotopic charge ($Z-Z_{\text{mp}}$) of fragments versus fractional yields of Nd and In isotopes and the Gaussian fitted curve through the data are shown in Figs. 7(a)–7(c). The dispersion parameters (W_Z) obtained by Gaussian fitting of the distribution of Nd and In isotopes are displayed in Table VI. The estimated width parameters (W_Z) for Nd isotopes are found to be 1.00 and 0.93 at $E_{\text{c.m.}} = 56.2$ and 53.4 MeV, respectively. Further, width parameter W_Z has been calculated by converting the parameter $W_{A'}$ of isotopic yield into W_Z using the following relation [6–8]

$$W_Z = \left(\frac{W_{A'}}{A'} \right) Z \quad (4)$$

The calculated values of W_Z are 1.0028 and 0.9205 for Nd isotopes at $E_{\text{c.m.}} = 56.2$ and 53.4 MeV, respectively, and 0.1573 for In isotopes at $E_{\text{c.m.}} = 56.2$ MeV, which are fairly close to values obtained from Figs. 7(a)–7(c), listed in Table VI.

D. Mass distribution of fission fragments

Different degrees of freedom of fission dynamics have been disentangled in heavy-ion-induced fission reactions using fission fragments' mass distribution in the past few years.

TABLE VI. The isobaric charge dispersion parameter obtained from the Gaussian fit (see Fig. 7) and using Eq. (4) at different excitation energies (E^*).

$E_{\text{c.m.}}$ (MeV)	E^* (MeV)	Isotope	W_Z from Fig. 7	W_Z from Eq. (4)
56.2	52.7	Nd	1.00 ± 0.23	1.0028
53.4	49.9	Nd	0.93 ± 0.27	0.9205
56.2	52.7	In	0.18 ± 0.01	0.1573

However, it has already been established that the main crux of mass distribution is to understand the effect of nuclear shell and pairing with increasing excitation energy, the impact of potential energy surface, and angular momentum in fission dynamics. The experimentally measured cross sections of the fragments obtained from $^{11}\text{B} + ^{181}\text{Ta}$ reaction have been plotted as a function of mass number at $E_{\text{c.m.}} = 58.8, 56.2, 55.4, 53.4, 51.8,$ and 50.4 MeV to observe the distribution of the fission fragments, as shown in Figs. 8(a) and 8(b). Although one can observe that significantly large cross sections were measured for the fission fragments ^{83}Br and ^{131}La at $E_{\text{c.m.}} = 58.8$ MeV energy compared to others, they represent the mass distribution fairly well. In this study, experimentally measured total fission cross sections (σ_T^f), which are the sum of individual fission fragments, are 589.9, 494.6, 379.0, 352.6, 144.4, and 166.6 mb at $E_{\text{c.m.}} = 58.8, 56.2, 55.4, 53.4, 51.8,$ and 50.4 MeV, respectively. However, theoretical fission cross sections obtained from statistical model codes EMPIRE and PACE [43] are either zero or small (in the range of $\approx \mu\text{b}$) within the energy range considered. Nevertheless, several experimental groups had reported the total fission cross sections in the range of ≈ 200 – 1000 mb from $^{19}\text{F} + ^{169}\text{Tm} \rightarrow ^{188}\text{Pt}^*$ [6], $^{12}\text{C} + ^{169}\text{Tm}, ^{186,187}\text{Re} \rightarrow ^{181}\text{Re}^*, ^{198,199}\text{Tl}^*$ [51], and $^{16}\text{O} + ^{181}\text{Ta} \rightarrow ^{197}\text{Tl}^*$ [8], etc., systems, which are populating compound nuclei in the same mass range.

In general, the CN formed in the heavy-ion-induced reaction carries higher excitation energy than the fission barrier, which yields the symmetric mass distribution. The mass distribution of fission fragments are broad and symmetric and can be fitted grossly with Gaussian distribution leaving a few points aside, as shown in Figs. 8(a) and 8(b). A little broad Gaussian mass distribution is acceptable, and it indicates that the populated post fission fragments are from compound nuclear mechanism. The upward arrows used in Figs. 8(a) and 8(b) indicate that the fission fragments, which are populating in metastable state, have been measured and the total production cross sections of those fragments are expected to be large. The dispersion parameters of fission fragments mass distribution such as width parameter (W_M) and most probable mass (W_{mp}) have been extracted from Gaussian fitting, and are found to be 18.0 and 104 at $E_{\text{c.m.}} = 58.8$ MeV; 16.3 and 105 at $E_{\text{c.m.}} = 56.2$ MeV; 15.8 and 104 at $E_{\text{c.m.}} = 55.4$ MeV; 14 and 104 at $E_{\text{c.m.}} = 53.4$ MeV; 12.3 and 104 at $E_{\text{c.m.}} = 51.8$ MeV; 11.9 and 104.3 at $E_{\text{c.m.}} = 50.4$ MeV. The variance of mass and charge distribution could easily be understood for the compound nucleus with $(Z^2/A) < 36$,

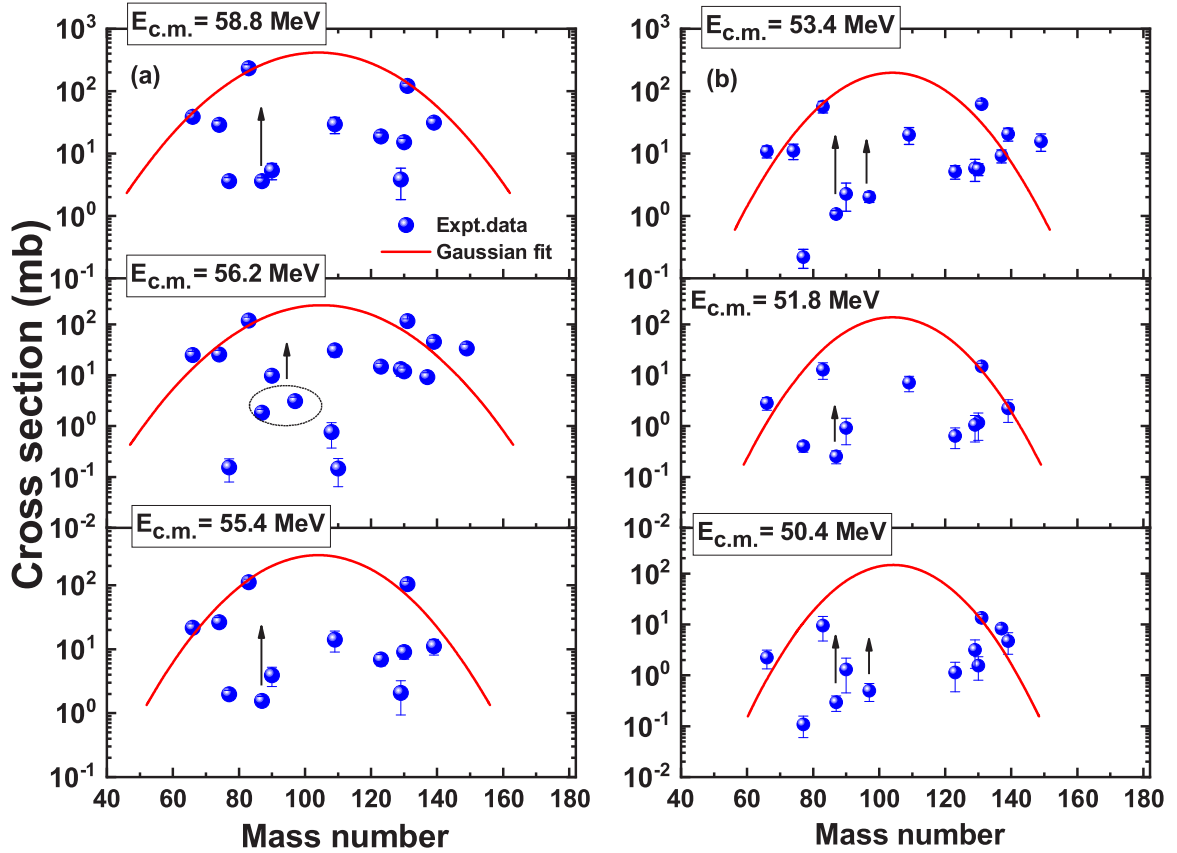


FIG. 8. Mass distribution of fission fragments (a), (b) produced via complete and incomplete fusion-fission processes in $^{11}\text{B} + ^{181}\text{Ta}$ reaction at different incident energies. Red line represents the Gaussian fit.

discussed in Refs. [13,14]. Interestingly the value of Z^2/A for the present reaction, $^{11}\text{B} + ^{181}\text{Ta}$, is 31.69, which is less than 36 for the CN ^{192}Pt . The variance of mass distribution W_M^2 have been found to be $324 u^2$ at $E_{c.m.} = 58.8$ MeV ($E^* = 55.3$ MeV), $266 u^2$ at $E_{c.m.} = 56.2$ MeV ($E^* = 52.7$ MeV), $250 u^2$ at $E_{c.m.} = 55.4$ MeV ($E^* = 51.9$ MeV), $196 u^2$ at $E_{c.m.} = 53.4$ MeV ($E^* = 49.9$ MeV), $151 u^2$ at $E_{c.m.} = 51.8$ MeV ($E^* = 48.3$ MeV), and $142 u^2$ at $E_{c.m.} = 50.4$ MeV ($E^* = 47.0$ MeV) and shown in Fig. 9. It is observed that the variance of mass distribution is increasing with raising excitation energy. However, the mass variance reported for the reaction $^{19}\text{F} + ^{169}\text{Tm}$ [6] populating the CN ^{188}Pt is $\approx 242 u^2$ at 58.5 MeV excitation energy, while we have found the mass variance $324 u^2$ at 55.3 MeV excitation energy for $^{11}\text{B} + ^{181}\text{Ta}$ reaction, which populated CN ^{192}Pt . This difference in the mass variance at a similar excitation energy can be understood in terms of entrance channel mass asymmetry $\alpha = (M_T - M_P)/(M_T + M_P)$. The α values are 0.80 and 0.89 for $^{19}\text{F} + ^{169}\text{Tm}$ and $^{11}\text{B} + ^{181}\text{Ta}$ reactions, respectively. It is explained in the literature that mass variance increases with increasing mass asymmetry at a given energy [6,8].

However, apart from the excitation energy of CN, the input angular momentum of CN directly influence the fission barrier. As the angular momentum increases, the saddle point becomes more compact and lowers the fission barrier. Therefore, for a particular E^* , CN's higher angular momentum has higher fission probability. Hence, we have estimated the

excitation energy and maximum input angular momentum of CN ^{192}Pt formed in $^{11}\text{B} + ^{181}\text{Ta}$ reaction; they are 47.0 MeV and $19\hbar$, 48.3 MeV and $21\hbar$, 49.9 MeV and $23\hbar$, 51.9 MeV and $26\hbar$, 52.7 MeV and $27\hbar$, and 55.3 MeV and $30\hbar$ at projectile energies $E_{c.m.} = 50.4, 51.8, 53.4, 55.4, 56.2,$ and 58.8 MeV, respectively.

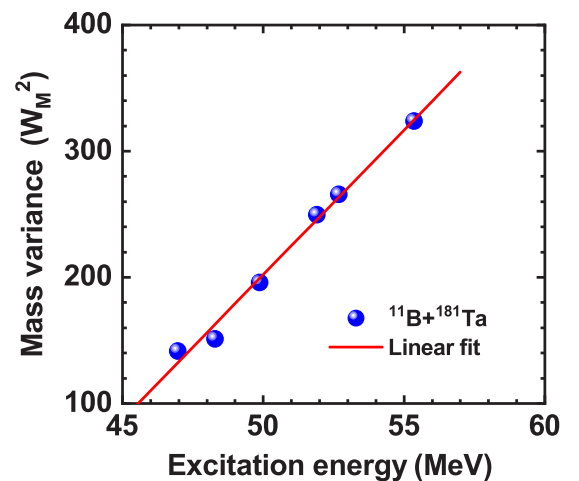


FIG. 9. The mass variance of fission fragments' mass distribution plotted as a function of excitation energy (E^*) for the $^{11}\text{B} + ^{181}\text{Ta}$ reaction. Solid red line shows the linear fit of data.

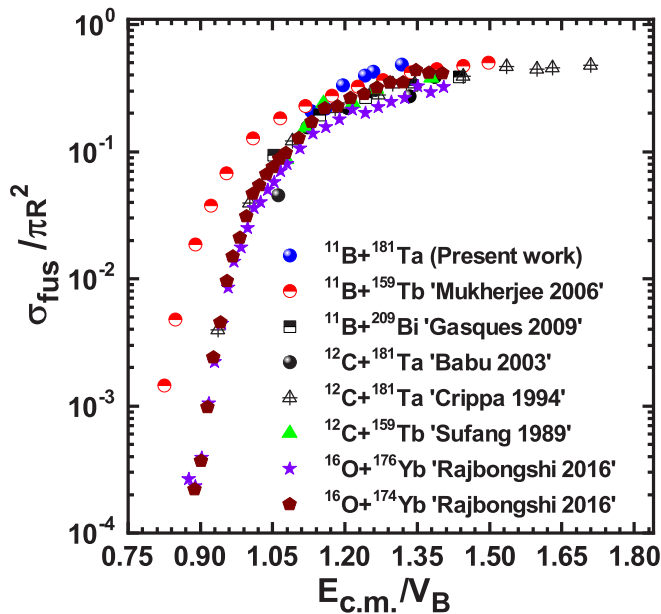


FIG. 10. Comparison of the reduced fusion excitation function of $^{11}\text{B} + ^{181}\text{Ta}$ system with similar systems such as $^{11}\text{B} + ^{159}\text{Tb}$; Mukherjee 2006 [23], $^{11}\text{B} + ^{209}\text{Bi}$; Gasques 2009 [3], $^{12}\text{C} + ^{181}\text{Ta}$; Babu 2003 [24], $^{12}\text{C} + ^{181}\text{Ta}$; Crippa 1994 [25], $^{12}\text{C} + ^{159}\text{Tb}$; Sufang 1989 [26], and $^{16}\text{O} + ^{174,176}\text{Yb}$; Rajbongshi 2016 [27].

E. Comparison with other systems in the similar compound nucleus mass range

A comparison has been made between the measured complete fusion that includes the sum of residues produced from complete fusion and fusion-fission processes in $^{11}\text{B} + ^{181}\text{Ta}$ reaction with other systems having a similar mass range of compound nucleus, such as $^{11}\text{B} + ^{159}\text{Tb}$ [23], $^{11}\text{B} + ^{209}\text{Bi}$ [3], $^{12}\text{C} + ^{181}\text{Ta}$ [24], $^{12}\text{C} + ^{181}\text{Ta}$ [25], $^{12}\text{C} + ^{159}\text{Tb}$ [26], and $^{16}\text{O} + ^{174,176}\text{Yb}$ [27] as presented in Fig. 10. It can be observed that the fusion cross sections (σ_{fus}) and $E_{\text{c.m.}}$ are scaled by the maximum geometrical cross section (πR^2) and Bass-barrier height (V_B), respectively. The method has been adopted to incorporate the differences in nuclear radius and barrier position of different systems to make a comparison between them [52]. We have measured the excitation function within $E_{\text{lab}} = 53\text{--}63$ MeV ($E_{\text{c.m.}} = 50\text{--}59$ MeV), the above barrier energy region, while fusion cross section have been measured at above and below barrier region in $^{11}\text{B} + ^{159}\text{Tb}$, $^{12}\text{C} + ^{181}\text{Ta}$, and $^{16}\text{O} + ^{174,176}\text{Yb}$ reactions. The contribution of CF and fission cross sections have been considered in $^{11}\text{B} + ^{209}\text{Bi}$

system. It can be observed from Fig. 10 that cross-section from all the compared systems are overlapping including our measured data in above barrier region. However, the CF cross sections measured by Mukherjee *et al.* [23] in $^{11}\text{B} + ^{159}\text{Tb}$ is larger than $^{16}\text{O} + ^{174,176}\text{Yb}$ [27] and $^{12}\text{C} + ^{181}\text{Ta}$ [25] systems in below barrier region. This difference in fusion cross sections can be understood in terms of the fusion Q value (Q_{fus}). The Q_{fus} for $^{11}\text{B} + ^{159}\text{Tb}$ is -0.099 MeV while Q_{fus} for $^{11}\text{B} + ^{209}\text{Bi}$, and $^{16}\text{O} + ^{174,176}\text{Yb}$ reactions are -19.86 , and -24.36 , -21.93 MeV, respectively. The more negative Q_{fus} value restricts the interacting partners to get fused, suggesting more fusion probability in the case of the $^{11}\text{B} + ^{159}\text{Tb}$ system as compared to others.

V. CONCLUSION

In the present article, we have reported the residues' cross sections populated via CF, ICF, and CF/ICF-fission processes in $^{11}\text{B} + ^{181}\text{Ta}$ reaction using the γ -spectroscopic technique within 4.8–5.7 MeV/nucleon energy range. Theoretical predictions from EMPIRE, which uses Hauser-Feshbach formalism for compound evaporation and the exciton model for PEQ reaction, and Hauser-Feshbach theory-based PACE code are in good agreement with the measured data from xn -channels; it confirms the production of those residues through the CF mechanism. However, enhanced cross-section observed in the α - and p -emitting channels above the theoretical prediction has been attributed to ICF of ^{11}B . Further, dispersion parameters from isotopic and isobaric yield distributions for neodymium and indium isotopes have been extracted from a single-peaked Gaussian distribution function and found to be in good agreement for neodymium isotopes with the literature values, whereas it is less for indium isotopes. The mass distributions of fission fragments are broad and symmetric, indicating fission fragments' production through the compound nucleus's de-excitation. The mass variance of fission fragments' mass distribution increases with increasing excitation energy for $^{11}\text{B} + ^{181}\text{Ta}$ reaction.

ACKNOWLEDGMENTS

We sincerely thank the BARC-TIFR Pelletron team for their assistance during the experiment. We also appreciate our colleagues from IIT Roorkee for their help and passionate teamwork. Research Grants No. 03(1467)/19/EMR-II from CSIR(IN), No. INT/RUS/RFBR/387 from DST(IN), and students' research fellowships from the MHRD, Government of India, are gratefully acknowledged.

[1] L. F. Canto, P. R. S. Gomes, R. Donangelo, J. Lubian, and M. S. Hussein, *Phys. Rep.* **596**, 1 (2015).
 [2] R. Prajapat and M. Maiti, *Phys. Rev. C* **101**, 064620 (2020).
 [3] L. R. Gasques, D. J. Hinde, M. Dasgupta, A. Mukherjee, and R. G. Thomas, *Phys. Rev. C* **79**, 034605 (2009).
 [4] G. S. Karapetyan, A. Deppman, V. Guimarães, A. Balabekyan, and N. A. Demekhina, *Phys. Rev. C* **94**, 024618 (2016).

[5] J. V. Kratz, J. O. Liljenzin, A. E. Norris, and G. T. Seaborg, *Phys. Rev. C* **13**, 2347 (1976).
 [6] M. Shuaib, V. R. Sharma, A. Yadav, S. Thakur, M. K. Sharma, I. Majeed, M. Kumar, P. P. Singh, D. P. Singh, R. Kumar *et al.*, *Phys. Rev. C* **99**, 024617 (2019).
 [7] G. K. Gubbi, A. Goswami, B. S. Tomar, A. Ramaswami, A. V. R. Reddy, P. P. Burte, S. B. Manohar, and B. John, *Phys. Rev. C* **59**, 3224 (1999).

- [8] V. R. Sharma, A. Yadav, P. P. Singh, M. K. Sharma, D. P. Singh, Unnati, R. Kumar, K. S. Golda, B. P. Singh, A. K. Sinha *et al.*, *Phys. Rev. C* **84**, 014612 (2011).
- [9] A. J. Sierk, *Phys. Rev. C* **33**, 2039 (1986).
- [10] K. Nishio, H. Ikezoe, Y. Nagame, M. Asai, K. Tsukada, S. Mitsuoka, K. Tsuruta, K. Satou, C. J. Lin, and T. Ohsawa, *Phys. Rev. Lett.* **93**, 162701 (2004).
- [11] A. C. Berriman, D. J. Hinde, M. Dasgupta, C. R. Morton, R. D. Butt, and J. O. Newton, *Nat. London* **413**, 144 (2001).
- [12] S. B. Manohar, A. Goswami, A. V. R. Reddy, B. S. Tomar, P. P. Burte, and S. Prakash, *Radiochim. Acta* **56**, 69 (1992).
- [13] S. B. Manohar, A. Goswami, and B. S. Tomar, *J. Radioanal. Nucl. Chem.* **203**, 331 (1996).
- [14] W. Reisdorf, M. de Saint-Simon, L. Remsberg, L. Lessard, C. Thibault, E. Roeckl, and R. Klapisch, *Phys. Rev. C* **14**, 2189 (1976).
- [15] M. de Saint-Simon, L. Lessard, W. Reisdorf, L. Remsberg, C. Thibault, E. Roeckl, R. Klapisch, I. V. Kuznetsov, Y. T. Oganessian, and Y. E. Penionshkevitch, *Phys. Rev. C* **14**, 2185 (1976).
- [16] A. C. Wahl, *J. Radioanal. Nucl. Chem.* **55**, 111 (1980).
- [17] S. Baba, H. Umezawa, and H. Baba, *Nucl. Phys. A* **175**, 177 (1971).
- [18] M. G. Itkis and A. Ya. Rusanov, *Phys. Part. Nucl.* **29**, 160 (1998).
- [19] G. N. Knyazheva, E. M. Kozulin, R. N. Sagaidak, A. Y. Chizhov, M. G. Itkis, N. A. Kondratiev, V. M. Voskressensky, A. M. Stefanini, B. R. Behera, L. Corradi *et al.*, *Phys. Rev. C* **75**, 064602 (2007).
- [20] R. Tripathi, K. Sudarshan, S. Sodaye, S. K. Sharma, and A. V. R. Reddy, *Phys. Rev. C* **75**, 024609 (2007).
- [21] D. Kumar and M. Maiti, *Phys. Rev. C* **95**, 064602 (2017).
- [22] A. Chauhan and M. Maiti, *Phys. Rev. C* **99**, 034608 (2019).
- [23] A. Mukherjee, S. Roy, M. K. Pradhan, M. S. Sarkar, P. Basu, B. Dasmahapatra, T. Bhattacharya, S. Bhattacharya, S. K. Basu, A. Chatterjee *et al.*, *Phys. Lett. B* **636**, 91 (2006).
- [24] K. S. Babu, R. Tripathi, K. Sudarshan, B. D. Shrivastava, A. Goswami, and B. S. Tomar, *J. Phys. G: Nucl. Part. Phys.* **29**, 1011 (2003).
- [25] M. Crippa, E. Gadioli, P. Vergani, G. Ciavola, C. Marchetta, and M. Bonardi, *Z. Phys. A* **350**, 121 (1994).
- [26] W. Sufang, C. Wei, and Z. Jiwen, *Chin. Phys.* **9**, 727 (1989).
- [27] T. Rajbongshi, K. Kalita, S. Nath, J. Gehlot, T. Banerjee, I. Mukul, R. Dubey, N. Madhavan, C. J. Lin, A. Shamlath *et al.*, *Phys. Rev. C* **93**, 054622 (2016).
- [28] R. Prajapat and M. Maiti, *Phys. Rev. C* **101**, 024608 (2020).
- [29] D. Kumar, M. Maiti, and S. Lahiri, *Phys. Rev. C* **96**, 014617 (2017).
- [30] D. Kumar, M. Maiti, and S. Lahiri, *Phys. Rev. C* **94**, 044603 (2016).
- [31] R. Prajapat, M. Maiti, D. Kumar, and A. Chauhan, *Phys. Scr.* **95**, 055306 (2020).
- [32] M. Maiti and S. Lahiri, *Phys. Rev. C* **84**, 067601 (2011).
- [33] M. Maiti, *Phys. Rev. C* **84**, 044615 (2011).
- [34] A. Chauhan, M. Maiti, and S. Lahiri, *Phys. Rev. C* **99**, 064609 (2019).
- [35] M. Maiti and S. Lahiri, *Radiochim. Acta* **99**, 359 (2011).
- [36] D. Kumar, M. Maiti, and S. Lahiri, *Sep. Sci. Technol.* **52**, 2372 (2017).
- [37] M. Maiti and S. Lahiri, *Radiochim. Acta* **103**, 7 (2015).
- [38] M. Maiti, *Radiochim. Acta* **101**, 437 (2013).
- [39] J. F. Ziegler, M. D. Ziegler, and J. P. Biersack, *Nucl. Instrum. Methods Phys. Res. B* **268**, 1818 (2010).
- [40] B. Wilken and T. A. Fritz, *Nucl. Instrum. Methods* **138**, 331 (1976).
- [41] J. Kemmer and R. Hofmann, *Nucl. Instrum. Methods* **176**, 543 (1980).
- [42] M. Herman, R. Capote, B. V. Carlson, P. Oblozinsky, M. Sin, A. Trkov, H. Wienke, and V. Zerkin, *Nucl. Data Sheets* **108**, 2655 (2007).
- [43] A. Gavron, *Phys. Rev. C* **21**, 230 (1980).
- [44] A. Gilbert and A. G. W. Cameron, *Can. J. Phys.* **43**, 1446 (1965).
- [45] A. V. Ignatyuk, J. L. Weil, S. Raman, and S. Kahane, *Phys. Rev. C* **47**, 1504 (1993).
- [46] A. D'Arrigo, G. Giardina, M. Herman, A. V. Ignatyuk, and A. Taccone, *J. Phys. G: Nucl. Part. Phys.* **20**, 365 (1994).
- [47] R. Bass, *Nucl. Phys. A* **231**, 45 (1974).
- [48] C. M. Perey and F. G. Perey, *At. Data Nucl. Data Tables* **17**, 1 (1976).
- [49] A. Bail, O. Serot, L. Mathieu, O. Litaize, T. Materna, U. Köster, H. Faust, A. Letourneau, and S. Panebianco, *Phys. Rev. C* **84**, 034605 (2011).
- [50] A. C. Wahl, *Phys. Rev.* **99**, 730 (1955).
- [51] J. Gilmore, S. G. Thompson, and I. Perlman, *Phys. Rev.* **128**, 2276 (1962).
- [52] Z. Kohley, J. F. Liang, D. Shapira, R. L. Varner, C. J. Gross, J. M. Allmond, A. L. Caraley, E. A. Coello, F. Favela, K. Lagergren *et al.*, *Phys. Rev. Lett.* **107**, 202701 (2011).
- [53] National Nuclear Data Center, Brookhaven National Laboratory, <http://www.nndc.bnl.gov/nudat2>.
- [54] S. Y. F. Chu, L. P. Ekström, and R. B. Firestone, The Lund/LBNL Nuclear Data Search: WWW Table of Radioactive Isotopes, <http://nucleardata.nuclear.lu.se/toi/>.